Journal of Alloys and Compounds 1028 (2025) 180612

Contents lists available at ScienceDirect

Journal of Alloys and Compounds

journal homepage: www.elsevier.com/locate/jalcom

The evolution of redox potentials in pyrochlore-based intercalation anodes for potassium-ion batteries

Mikhail Yu. Tashlanov [a,*], Dmitry A. Aksyonov [a], Sergey N. Marshenya [a], Ivan V. Mikheev [b], Evgeny V. Antipov [a,b], Stanislav S. Fedotov [a,*]

[a] Skoltech Center for Energy Science and Technology, Skolkovo Institute of Science and Technology, Bolshoy Boulevard, 30, bld. 1, Moscow 121205, Russia
[b] Department of Chemistry, Lomonosov Moscow State University, 1-3 Leninskie Gory, Moscow 119234, Russia

ARTICLE INFO

Keywords:
Defect pyrochlore
Potassium-ion batteries
Anode

ABSTRACT

Tungsten oxides and related compounds have been known as negative electrode materials for metal-ion batteries for decades. Despite their structural flexibility, most studies has largely focused on lithium-based energy storage systems. Here, we investigated $KM_xW_{2-x}O_6$ (M = Ta, Nb, Ti, Cr, Al) oxides adopting a defect pyrochlore structure as intercalation-type anodes for potassium-ion batteries. Crystal structure, chemical composition, and thermal behavior of all representatives were comprehensively characterized. Electrochemical testing in K half-cells revealed average operating potentials of the considered pyrochlores to be in the range of ~1.1–1.3 V vs. K^+/K, consistent with density functional theory predictions. The variation in the electrochemical performance among the $KM_xW_{2-x}O_6$ was correlated with differences in electronic conductivity of M dopants, as validated by M density of states calculations. Through regression analysis of Rietveld-refined structural data, a strong linear dependence ($\rho = 0.96$) between the average intercalation potential of $KM_xW_{2-x}O_6$ and the intrinsic parameters (ionic radius and electronegativity) of the M metal was established. This work not only advances fundamental understanding of tungsten-based oxygen-deficient pyrochlores but also paves the way for their development as potassium-ion intercalation hosts.

1. Introduction

Potassium-ion batteries (PIBs) have emerged as a promising energy storage technology due to the abundance and low cost of K precursors along with the electrochemical performance comparable to lithium-ion batteries (LIBs). Among the various materials explored as electrodes for PIBs, inorganic intercalation compounds have attracted significant attention. Their rigid frameworks minimize structural expansion upon alkali cation (de)insertion, ensuring excellent mechanical stability during electrochemical cycling. As a result, developing new inorganic host structures remains an important research focus in battery science today.

The structural flexibility of tungsten oxides (WO_{3-x}) – including the formation of oxygen vacancies [1,2], the incorporation of a different dopants into their framework [3,4], and the intercalation of ions into their voids [5,6] – has enabled a wide range of applications. In particular, these materials reveal gas-sensing, thermochromic, photocatalytic, superconducting, and electrochemical properties [7–14]. In the context of electrochemical behavior, the different modifications of tungsten trioxide (hexagonal [15,16], monoclinic [17,18], and pyrochlore-type WO_3 [19,20]) along with related compounds (Nb-W-O shear structures [21] and bronze-like phases [22,23]) have been extensively investigated as negative electrodes for LIBs. Nevertheless, research on W-containing oxides as electroactive materials for other metal-ion batteries remains relatively limited [24–27].

Recently, it was demonstrated that a $KNbWO_6$ compound can reversibly (de)intercalate K^+ at a ~1.25 V vs. K^+/K average operating potential (AOP) [28]. Extended and high-power testing of such anode material in potassium half-cells showed its impressive electrochemical stability. The highlighted Nb-containing composition belongs to the $KM_xW_{2-x}O_6$ (M = Nb, Ta, Ti, Cr, Al) family of so-called defect pyrochlores, where dopant (M) substitutes W in varying concentrations. Some of these pyrochlores were known to exhibit high ionic conductivity – for example, $KTi_{0.5}W_{1.5}O_6$ demonstrates $\sigma(K^+) \sim 2.5 \bullet 10^{-3}$ $S \bullet cm^{-1}$ at 300 °C [29]. These experimental findings align well with theoretical observations of 3D isotropic K^+ diffusion network and low migration barriers (~0.4 eV) in the $KNbWO_6$ framework [28]. Given the

* Corresponding authors.
E-mail addresses: Mikhail.Tashlanov@skoltech.ru (M.Yu. Tashlanov), S.Fedotov@skoltech.ru (S.S. Fedotov).

https://doi.org/10.1016/j.jallcom.2025.180612
Received 1 March 2025; Received in revised form 13 April 2025; Accepted 23 April 2025
Available online 24 April 2025

structural similarities of the $KM_xW_{2-x}O_6$ compounds and the suggested role of W^{6+}/W^{5+} redox transformations as the main reason of $KNbWO_6$ electrochemical activity, we assumed that other tungsten-based pyrochlores should also display redox behavior in potassium-ion batteries.

In this paper, we expand the range of electrochemically active $KM_xW_{2-x}O_6$ (M = Ta, Ti, Cr, Al) defect pyrochlores, evaluating them as novel intercalation-type anodes for potassium-ion batteries (PIBs). The above compounds were comprehensively characterized with structural, compositional, and theoretical methods. Their electrochemical behavior was compared with the previously reported $KNbWO_6$ pyrochlore-based anode. We found that all studied systems demonstrate electrochemical activity in the low-potential region (~1.1–1.3 V vs. K^+/K), attributed to W^{6+}/W^{5+} redox transitions during K^+ (de)intercalation. The observed AOP shift in $KM_xW_{2-x}O_6$ upon substitution of W with M metals was correlated with structural data (interatomic distances and angles related to $[M/WO_6]_\infty$ frameworks) and fundamental parameters of the M^{x+}, *i.e.,* electronegativity and ionic radii. Symbolic regression analysis revealed a strong linear dependence ($\rho = 0.96$) between these intrinsic characteristics and the experimentally obtained data. Additionally, density functional theory (DFT) calculations results – including average intercalation potentials and the density of states of M in pyrochlores – are in good agreement with the electrochemical behavior of $KM_xW_{2-x}O_6$ anodes in galvanostatic experiments. This work advances our understanding on the structural and electrochemical properties of the $KM_xW_{2-x}O_6$ pyrochlores, highlighting their prospects as novel negative electrodes for PIBs.

2. Experimental

2.1. Synthesis

- Pyrochlores

The $KM_xW_{2-x}O_6$ (M = Ta, Nb, Ti, Cr, Al; x = 1, 0.5, 0.33) samples were synthesized by a solid state reaction of the following reactants in stoichiometric quantities: $K_2C_2O_4\times H_2O$ (Sigma Aldrich, 99.9 %), WO_3 (Redkiy Metal, 99.9 %) and Ta_2O_5 (Redkiy Metal, 99.9 %), Nb_2O_5 (Redkiy Metal, 99.9 %), TiO_2 (Sigma Aldrich, 99.9 %), $Cr(NO_3)_3\times 9H_2O$ (Ruskhim, 99.9 %), $Al(NO_3)_3\times 9H_2O$ (Ruskhim, 99.9 %), correspondingly. Initial mixtures were thoroughly ground in a SPEX PrepMill high-energy mill during 1 h and annealed at 400 °C for 12 h in air followed by regrinding of the intermediate product during 1 h and annealing at 650 °C for 12 h in air to obtain final compositions.

- Prussian blue analogue

$K_2FeFe(CN)_6$ was obtained by the following procedure [30]. The solution of KCl (0.2 mol; Sigma Aldrich, ReagentPlus, ≥99.0 %) and $K_4Fe(CN)_6\times 3H_2O$ (0.005 mol; Sigma Aldrich, BioUltra, ≥99.5 %) in 100 mL of H_2O (dist.) was added dropwise at a speed of 1 drop per 3 s to the solution of $FeSO_4\times 7H_2O$ (0.005 mol; Sigma Aldrich, ReagentPlus, ≥99 %) in 50 mL of H_2O (dist.). The resulting solution was magnetically stirred at 500 rpm for 2 h at 25 °C to complete the reaction. The dark blue precipitate was centrifuged with an EtOH:H_2O (1:1 v:v) mixture 5 times and then dried under the dynamic vacuum at 70 °C for 12 h.

2.2. Materials characterization

- Powder X-ray diffraction (PXRD)

PXRD data of pyrochlores were acquired from a Bruker D8 ADVANCE diffractometer (Cu-K_α radiation, 10–130° 2θ range, 0.020° s^{-1} scanning rate). PXRD pattern of $K_2FeFe(CN)_6$ (K-FeHCF) was recorded with a Guinier camera Huber G670 powder diffractometer (Co-$K_{\alpha1}$ radiation, 4–100° 2θ range).

- Crystal structure refinement

The Le Bail fit (K-FeHCF) and the Rietveld refinement (pyrochlores) were carried out with the Jana2006 program package [31]. A set of Chebyshev polynomials and pseudo-Voight function were used for the background and peak shape fitting, correspondingly. At the first step of Rietveld refinement, the stoichiometry of the Nb/W (16*c*) site from the $KNbWO_6$ structure [32] were brought to the corresponding M/W ratio according to the ICP-OES results for all pyrochlores under study. Then, K and O (H_2O) positions were determined using the three-dimensional difference Fourier maps (the occupancy of the K sites was normalized to the ICP-OES results as well). The O (H_2O) occupancy was set based on the thermogravimetric (TG) data. The atomic displacement parameters for M and W were equated and processed together. The refined $KM_xW_{2-x}O_6$ structures were visualized using VESTA software [33]. The regression analysis of structural data and fundamental parameters was performed via the PySR Regression tool [34].

- Scanning electron microscopy (SEM)

The morphology and elemental composition of pyrochlores' powders were investigated using Quattro S scanning electron microscopy (Thermo Fisher Scientific, LaB_6 field emission cathode) with an EDS Bruker XFlash 6160 energy-dispersive detector in a secondary electron mode with an accelerating voltage of 15 kV and 0.69 nA current.

- Elemental analysis (ICP-OES)

Elemental ratios in the pyrochlores' powders were determined with an axial view ICP-OES spectrometer Agilent 720 (Agilent, Australia). The analysis was conducted after digestion of the compositions (ca. 50 mg) in the mixture of conc. HNO_3:HF (5:1 by vol.) for 2 h at 60 ℃. The samples were then diluted to the volumetric flask's calibration mark. To improve the reproducibility of the results, the internal standard (Sc solution 20 ppm) was used, which premixed in an on-line mode to the analyzed samples.

- Thermogravimetric analysis (TG-DSC)

Thermal analysis was carried out with a TG-DSC F3 STA-449 apparatus (Netzsch) combined with a mass spectrometer QMS 403 D Aëolos (Netzsch) under Ar or dry air flow (50 mL•min^{-1}). The powders were heated at 10 K•min^{-1} rate in the 30–800 °C temperature range. The residual carbon content in the $KM_xW_{2-x}O_6$/C was estimated to be ~6 wt.% by TGA-MS results [28].

- Raman spectroscopy

The Raman spectra were recorded using a DXRxi Raman Imaging Microscope (Thermo Fisher) using 532 nm laser excitation (laser power at sample plane ca. 1.5 mW, exposure time 0.1 s, averaging by 50 scans).

2.3. Electrochemical measurements

- Carbon coating process and electrode preparation

Prior to the electrochemical testing, all pristine pyrochlore powders were carbon-coated with polyacrylonitrile (PAN, M_w ~ 5000 g•mol^{-1}) as a carbon precursor according to the described procedure [35]. The electrodes were prepared by mixing $KTaWO_6$/C, $KNbWO_6$/C, $KTi_{0.25}W_{1.5}O_6$/C, $KCr_{0.33}W_{1.67}O_6$/C, $KAl_{0.33}W_{1.67}O_6$/C powders (80 wt.%), carbon Super-P (10 wt.%) and polyvinylidene fluoride (pVdF, Sigma-Aldrich) as a binder (10 wt.%). N-methyl pyrrolidinone (NMP, Sigma-Aldrich, anhydrous, 99.5 %) was added to dissolve pVdF. The resulting slurry was cast on aluminum foil (20 μm, 99.9 %, Tob New Energy, China) by a Doctor Blade technique (100–200 μm thickness), dried at 70 °C and calendared. The 15 mm disks were cut from electrode tape and then dried under the dynamic vacuum at 120 °C for 12 h to remove residual NMP. The active material loading after drying varied from ~0.5 mg•cm^{-2} (to minimize the thickness and porosity effects of the composite on further measurements in three-electrode configuration cells) to ~3 mg•cm^{-2} (for regular testing in two-electrode cells).

- Cell assembling and electrochemical testing in two-electrode configuration

The electrochemical properties of defect pyrochlores were evaluated

using Swagelok-type and coin-type two-electrode cells with Al current collectors, 2.5 M KPF_6 (KPF_6, dried under vacuum for 24 h at 80 °C, Alfa-Aesar, 99.5 %) in diglyme (Sigma-Aldrich, anhydrous) as electrolyte [36] in the amount of 150 μL (Swagelok-type) and 100 μL (coin-type), glass-fiber separators (Whatman, thickness 260 μm, 1.6 μm pore size) and K metal (Sigma-Aldrich, chunks, roll-pressed into ~100 μm foil and cut as 15 mm disks) used as both counter electrode (CE) and reference electrodes (RE). The cyclic voltammetry and

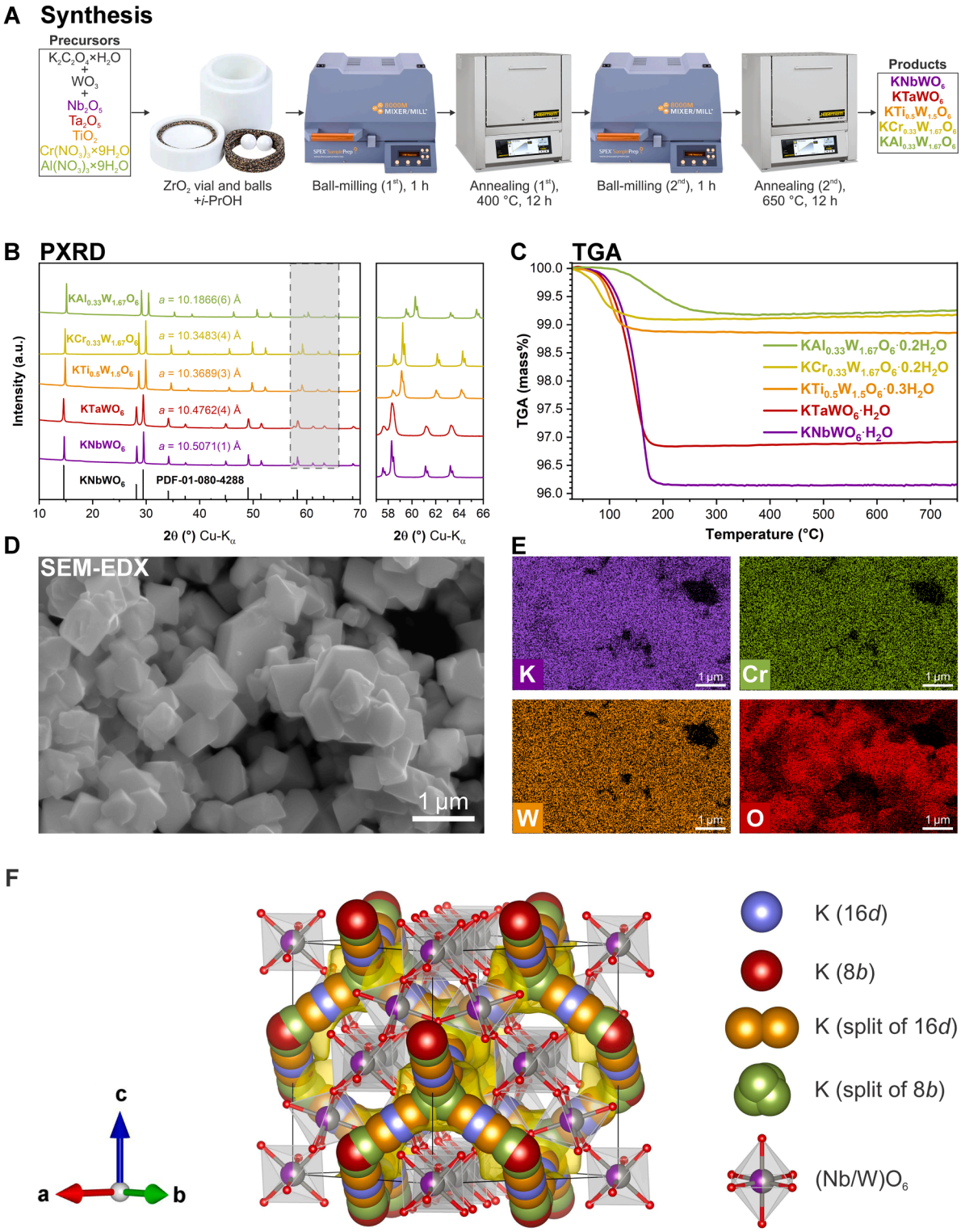

Fig. 1. (A) Schematic diagram of $KM_xW_{2-x}O_6$ solid-state synthesis. (B) PXRD patterns of $KM_xW_{2-x}O_6 \bullet H_2O$. For better visualization of the peaks shift when moving from one M metal to another, an enlarged area (gray rectangular) is shown on the right. (C) TGA curves for $KM_xW_{2-x}O_6 \bullet H_2O$. (D) SEM image of $KCr_{0.33}W_{1.67}O_6$ (50kX magnification) and (E) corresponding color-coded elemental maps of K, Cr, W, and O. (F) $KNbWO_6$ framework with superposition of all available K sites (16*d*, 8*b* and two types of 32*e*) and superimposed isosurface (yellow) from the BVEL calculations [28,45]. Potassium positions are shown with full occupancy for ease of perception, while in the real structure of $KNbWO_6$ these sites are partially occupied, with the exception of 8*b*.

galvanostatic measurements were carried out at 22 ± 1 °C using a Biologic VMP3 and NEWARE potentiostat, correspondingly. The specific capacity and current were calculated based on the mass of pyrochlores' powders.

- Cell assembling and electrochemical testing in three-electrode configuration

The expected high reactivity of metallic K with most of electrolytes typically lead to strong polarization at the CE which can result in an electrode potential change for two-electrode cells and therefore misinterpretation of the data. To exclude the polarization contribution, cyclic voltammetry of $KNbWO_6$/C as a model system was also carried out in a three-electrode configuration, where $K_2FeFe(CN)_6$ was used as a RE. The ratio of active component, carbon Super-P and binder (PVDF) in such RE was chosen as 70:10:20 wt.% [37]. The procedure for preparing reference electrodes was similar to that described above. The amount of electrolyte used in three-electrode cells was 200 μL. The loading of $K_2FeFe(CN)_6$ in dried electrodes was in the range of ~0.9–1.1 mg•cm^{-2}.

Before examining the $KNbWO_6$/C pyrochlore in the three-electrode cell configuration, the preliminary galvanostatic cycling of the PBA-based material was performed in a two-electrode regime, *i.e.*, $K_2FeFe(CN)_6$ was used as a working electrode (WE) and metallic K as both CE and RE. The two wide plateaus with constant potentials at charge-discharge curves correspond to biphasic regions, as expected. Then, the $K_2FeFe(CN)_6$ electrode was charged to the middle of the 1st plateau (~3.382 V vs. K^+/K) and held at this potential for ~2 h until the current reached 1 nA. Finally, the cyclic voltammetry at a 0.1 mV•s^{-1} scanning rate was carried out in the following configuration: $KNbWO_6$/C – WE, $K_2FeFe(CN)_6$ – RE, metallic K – CE.

2.4. DFT calculations

The density functional theory (DFT) calculations were performed using the projected augmented plane wave method with the Vienna ab initio simulation package (VASP) [38] and the high-throughput Python-based package SIMAN [39]. We employed the generalized gradient approximation (GGA) for the exchange-correlation functional, along with standard PAW PBE potentials [40], using the minimum number of valence electrons. To account for the strongly correlated nature of Nb's and Cr's *d*-electrons, a Hubbard-like correction was applied using the Dudarev scheme [41] with a *U* value of 1.5 eV and 3.5 eV, respectively. To improve the description of intercalation potentials, a hybrid exchange-correlation functional, HSE06 was used. Gaussian smearing, with a width of 0.1 eV, was used for Brillouin-zone integrations. All calculations were spin-polarized and assumed a ferromagnetic ground state. The energy cutoff was set to 400 eV, and a Gamma-centered k-point mesh with a spacing of at least 0.3 Å^{-1}. The cluster expansion method, as implemented in the ATAT code, was used to study phase stabilities [42]. The root mean square error of the energies from the resulting cluster expansion Hamiltonian compared to DFT energies was estimated to be less than 0.05 eV per K ion.

3. Results

3.1. Synthesis and characterization

A number of pyrochlore-type compounds $KM_xW_{2-x}O_6$ (M = Ta, Nb, Ti, Cr, Al) have been obtained via a conventional solid-state method (Fig. 1**A**) [29]. The selection was done based on the available compositional and structural opportunities of the framework to accommodate M metals with the 3+/4+/5+ oxidation states in corresponding M/W ratios.

The as-prepared samples were identified as single-phase with no impurities detected. The PXRD patterns of $KM_xW_{2-x}O_6$ were initially fitted by Le Bail method (Figure S1) using a cubic unit cell (S.G. *Fd*-3*m*). A raise in the unit cell parameters and the resulting shift of the diffraction peaks of pyrochlores to the left (Fig. 1**B**) when moving from Al-doped to Nb-doped composition is associated with the increase of the following parameters: (1) the ionic radius of the substituent M and the corresponding M/W–O bond lengths, (2) the contribution of the M in the M/W ratio, (3) the water content stored within the network of voids, since $KM_xW_{2-x}O_6$ exist as hydrates in air [29,43]. The amount of water was determined by TGA (Fig. 1**C**) for further structural refinement. Scanning electron microscopy (Fig. 1**D, S2**) revealed the morphology of pyrochlores powders presenting random shapeless agglomerates, where primary particles are octahedra of different sizes and degrees of distortion: from well-formed ($KTi_{0.5}W_{1.5}O_6$ and $KCr_{0.33}W_{1.67}O_6$) to highly-flattened ($KTaWO_6$, $KNbWO_6$, $KAl_{0.33}W_{1.67}O_6$) ones. A SEM-EDX data (Figure S3) showed that K, M (M = Ta, Nb, Ti, Cr, Al), W, and O are evenly distributed within particles of the synthesized materials following the expected chemical formula. The elemental maps of $KCr_{0.33}W_{1.67}O_6$ being shown as an example on the Fig. 1**E.** The stoichiometric ratio of metals in all studied pyrochlores were also confirmed with ICP-OES data (Table S1).

A notable feature of the considered compounds is the diversity and the mutual replacement of possible positions that potassium and oxygen (from H_2O) can occupy in the tungsten-based pyrochlore structure [32, 43,44]. Therefore, K and O (H_2O) positions during the Rietveld refinement were determined using three-dimensional difference Fourier maps (Figure S4). According to the results, K is located at 16*d* ($KTaWO_6$, $KNbWO_6$) as well as in two types of 32*e* positions: splitting of 16*d* ($KTi_{0.5}W_{1.5}O_6$, $KCr_{0.33}W_{1.67}O_6$) and 8*b* ($KAl_{0.33}W_{1.67}O_6$) sites. The O (H_2O) positions in $KM_xW_{2-x}O_6$•yH_2O were determined from residual electron density as follows: 32*e* (M = Ta, Nb), 8*b* (M = Ti, Cr), and 16*d* (M = Al). This diversity of sites is accounted for the presence of spacious voids and system of 3D channels, which enables the co-existence of several "guest species" (*e.g.*, alkali cation, H_2O) in the pyrochlore framework. The shift of K positions after hydration along with the interchangeability of the K and O (H_2O) sites is also a signature of the high mobility of K^+ (the abovementioned high ionic conductivity of $KM_xW_{2-x}O_6$) and the weak bonding of water molecules within the pyrochlore structure. Using the $KNbWO_6$ framework as a structural model for considered W-based defect pyrochlores, all available K sites from the current refinements and literature data [32] were combined in Fig. 1**F**. Such a distribution of K^+ ions over all possible positions stems from their close energetics and fits well with the 3D migration network shown for $KNbWO_6$ structure by BVEL and DFT-NEB calculations [28].

3.2. Electrochemical measurements

Prior to electrode fabrication, the electronic conductivity of pyrochlore powders was enhanced using carbon coating with PAN as a precursor. Raman analysis of the $KM_xW_{2-x}O_6$ (Figure S5) reveal the G/D bands of the carbon coating as well as the expecting stretching bands within the pyrochlore framework. The ratio of D-band and G-band in the spectra indicates that the coating mainly consists of amorphous carbon.

Cyclic voltammetry (CV) of carbon-coated $KTaWO_6$/C, $KNbWO_6$/C, $KTi_{0.5}W_{1.5}O_6$/C, $KCr_{0.33}W_{1.67}O_6$/C, and $KAl_{0.33}W_{1.67}O_6$/C electrode materials (Fig. 2**A**) revealed redox activity in the low-voltage region with the AOP varied from 1.08 V vs. K^+/K for the Al-doped sample to 1.39 V vs. K^+/K for the Ta-doped sample in potassium half-cells. The reliability of such measurements in two-electrode cells with metallic K as both CE and RE was additionally verified by cyclic voltammetry of $KNbWO_6$/C as a model system in a three-electrode cell. In this mode, the PBA-based reference electrode (PXRD data are shown in the Figure S1F) with a stable potential allows avoiding the possible contribution of potassium polarization on the electrochemical properties of materials under consideration. According to the data obtained (Figure S6), the cell configuration does not make any noticeable contribution to the shape of the CV curve in case of the Nb-based pyrochlore material meaning that the electrode potential on the potassium metal RE/CE is not affected much in the electrolyte used and can be considered stable. Therefore, pyrochlores can be further reliably studied in two-electrode

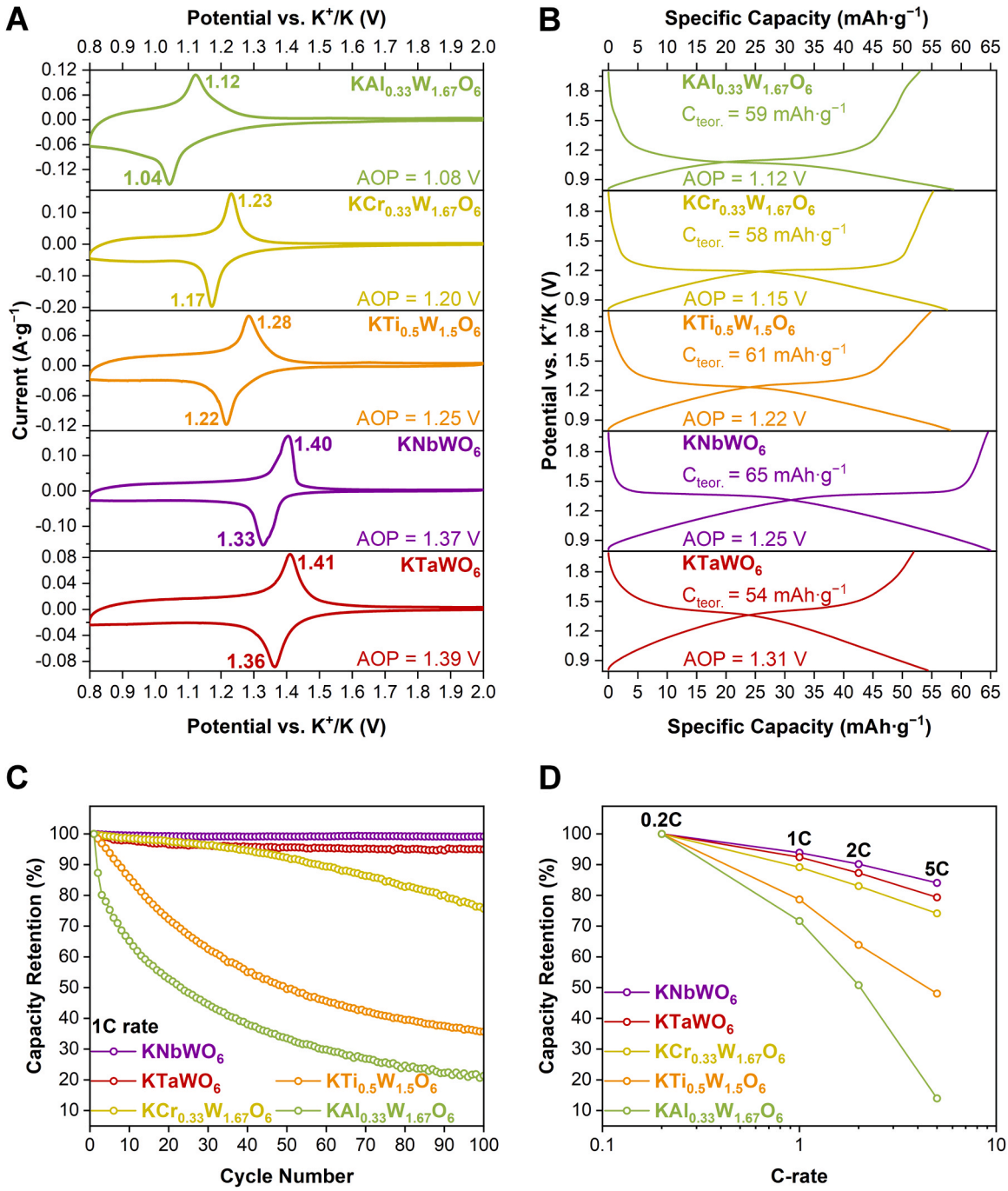

Fig. 2. Electrochemical characterization of $KM_xW_{2-x}O_6$/C pyrochlores in the K half-cells at 0.8–2 V potential range: (A) cyclic voltammograms at 0.1 mV•s^{-1} scan rate, (B) representative galvanostatic curves at 0.2C rate, (C) extended charge-discharge cycling at 1C rate, and (D) rate capability measurements from 0.2C to 5C rates (logarithmic scale on the X axis). The results of long-term cycling are normalized to the 1st cycle at 1C rate and do not take into account 3 preliminary formation cycles at 0.2C rate. The data for the $KNbWO_6$ electrochemical performance are taken from the [28].

configurations with metallic potassium as both RE and CE of sufficient stability.

Galvanostatic cycling at 0.2C rate (~12–13 mA•g^{-1}) demonstrated that the initial capacity of all pyrochlores is close to the theoretical values, *i.e.*, it corresponds to the (de)intercalation of 1 K mol-equivalent from the chemical formula according to the following equation: $KM_xW_{2-x}O_6/C + K^+ + \bar{e} \leftrightarrow K_2M_xW_{2-x}O_6/C$. Moreover, the AOP values were found in the range of 1.12–1.31 V vs. K^+/K (Fig. 2**B**) which are close to those derived from cyclic voltammetry.

According to the extended charge-discharge cycling results (Fig. 2**C** and **S8**), $KNbWO_6$ and $KTaWO_6$ are the most stable anode materials among the systems under consideration, with ~99 % (from 62.13 mAh•g^{-1} to 61.63 mAh•g^{-1}) and ~95 % (from 48.69 mAh•g^{-1} to 46.25 mAh•g^{-1}) capacity retention after 100 cycles at 1C rate. Besides, a decrease in capacity of ~24 % (from 52.13 mAh•g^{-1} to 39.8 mAh•g^{-1}) is observed for the $KCr_{0.33}W_{1.67}O_6$ pyrochlore, while the $KTi_{0.5}W_{1.5}O_6$ and $KAl_{0.33}W_{1.67}O_6$ materials show the noticeable deterioration of electrochemical performance with ~36 % (from 50.72 mAh•g^{-1} to 18.10 mAh•g^{-1}) and ~21 % (from 52.13 mAh•g^{-1} to 11.12 mAh•g^{-1}) capacity retention. Excluding the 1st cycles after C-rate changes, the Coulombic efficiency (Figure S8) was above 99 % for $KNbWO_6$, $KTaWO_6$, and $KCr_{0.33}W_{1.67}O_6$ samples whereas for

$KTi_{0.5}W_{1.5}O_6$ and $KAl_{0.33}W_{1.67}O_6$ pyrochlores Coulombic efficiency was found to be higher than 98 % and 97 %, correspondingly.

The highest capacity retention value after a 25-fold increase in current density (from 0.2C rate to 5C rate) during galvanostatic cycling (Fig. 2**D**, ***S7*** and ***S8***) was also demonstrated by $KNbWO_6$ (~84 %, from 64.95 mAh•g^{-1} to 54.61 mAh•g^{-1}) and $KTaWO_6$ (~79 %, from 53.90 mAh•g^{-1} to 42.73 mAh•g^{-1}) samples. While the $KCr_{0.33}W_{1.67}O_6$ pyrochlore loses a slightly more than a quarter of its initial capacity (~26 %, from 57.63 mAh•g^{-1} to 42.73 mAh•g^{-1}), significant fading with only ~48 % (from 60.46 mAh•g^{-1} to 29.06 mAh•g^{-1}) and ~14 % (from 58.71 mAh•g^{-1} to 8.2 mAh•g^{-1}) capacity retention was found for the $KTi_{0.5}W_{1.5}O_6$ and $KAl_{0.33}W_{1.67}O_6$ samples, correspondingly. Since the first few charge-discharge curves at 0.2C rate are formation cycles (for the growth of stable SEI), the Coulombic efficiency (Figure S8) there was ~90–91 % with a gradual increase to ~97–99 % for all the pyrochlores. As the current density increases to 5C and after returning to 0.2C rate, the Coulombic efficiency for Nb-, Ta-, and Cr-based materials reaches 99.5 % or higher, while for the Ti- and Al-containing sample the Coulombic efficiency varies from ~96 % to ~99.6 %.

Additionally, CV at different scan rates (Fig. 3**A**) were employed to evaluate the diffusion-controlled and (pseudo)capacitive contributions to K^+ storage in pyrochlore-type anodes. $KNbWO_6$ was selected as a model system due to its high electrochemical stability in previous measurements. Based on the relationship between scan rates and current response [$i(V) = av^b$], the b values (Fig. 3**B**, violet and red lines) for redox peak currents indicate mixed control ($0.35 \leq b \leq 0.7$ [46]). Meanwhile, the calculated b values in the 0.8–1.3 V region are close to 1 (Fig. 3**B**, green and orange lines), suggesting (pseudo)capacitive control here.

3.3. Regression analysis of structural and electrochemical parameters

The relationship between the different parameters [*e.g.*, bond lengths and angles obtained from the Rietveld refinement (Fig. 4**A**, Tables S2 and S3)] of $KM_xW_{2-x}O_6$ pyrochlores and the shift of their AOP obtained from galvanostatic cycling (GC) was determined using a symbolic regression analysis. The strongest correlation, with a value of 0.93, is observed between the working potential and the M/W–O bond distance, as shown in Table 1. However, the M/W–O bond length is not suitable for predictions, as it is itself a consequence of fundamental properties of the M metal such as ionic radii ($R_{ion.}$) and electronegativity (χ). Therefore, we utilize these parameters in the symbolic regression with the PySRRegressor tool to derive a formula that predicts the intercalation

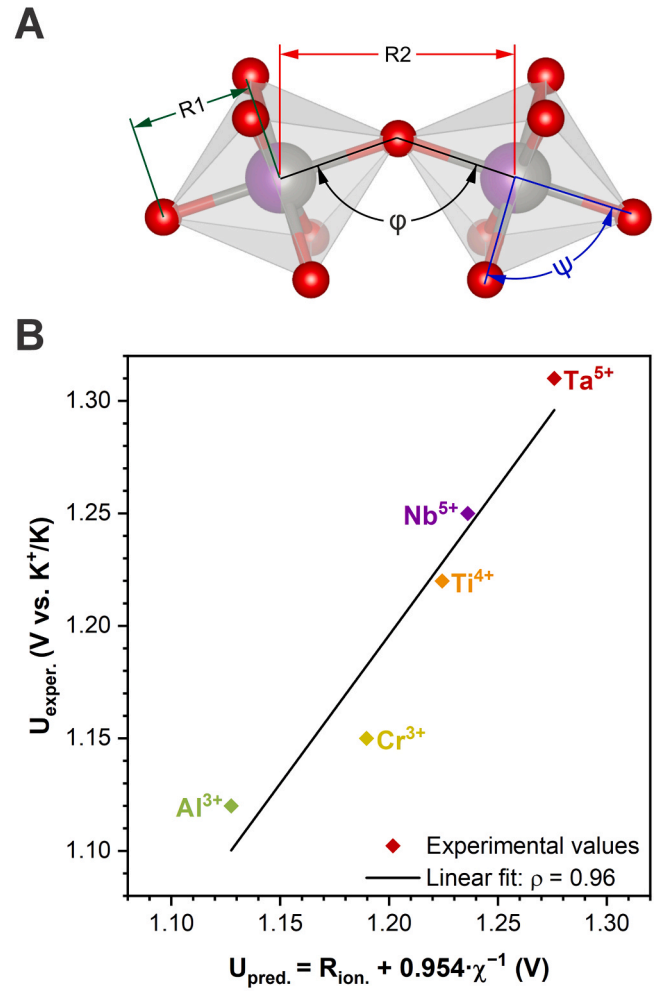

Fig. 4. (A) (Nb/W)O_6 octahedra connectivity motif in the $KNbWO_6$ as a model structure for other W-based pyrochlores. The highlighted bond lengths (R1, R2) and angles (φ, ψ) were used for the further regression analysis. (B) The dependence between K (de)intercalation potentials ($U_{exper.}$) obtained from GC data and predicted potential from symbolic regression analysis ($U_{pred.}$).

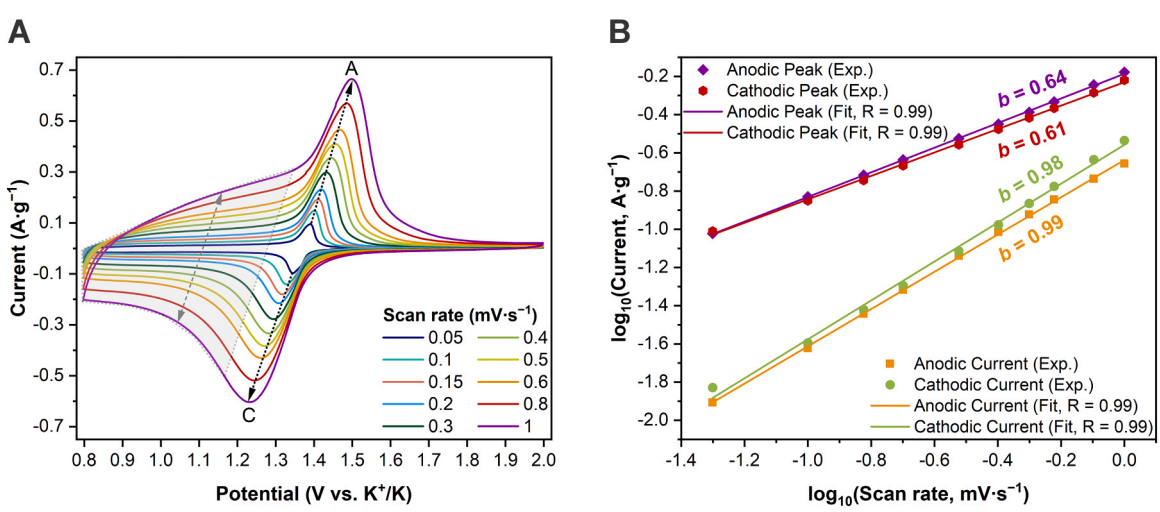

Fig. 3. (A) CV curves of $KNbWO_6$ at 0.05 – 1 mV•s^{-1} scan rates. The shaded area represents the pseudocapacitance region. (B) The calculated b values for the redox peak currents and the pseudocapacitive part at CVs. The current response for the linear fitting were selected taking into account the polarization effect when increasing the scan rate.

Table 1
Pearson correlation coefficient (ρ) between the AOP ($U_{aver.}$) obtained from the GC results and different parameters for $KM_xW_{2-x}O_6$ pyrochlores.

Feature	Pearson
$U_{aver.}$ (GC), V vs. K^+/K	1
R1 ($R_{M/W-O1}$), Å	0.93
R2 ($R_{M/W-M/W}$), Å	0.88
a, Å	0.88
R_{ion}. (Ionic radii of M in $KM_xW_{2-x}O_6$, CN = 6), Å	0.80
φ (angle M–O1–M), °	0.68
ψ (angle O1–M–O1), °	0.64
χ (Pauling electronegativity), $eV^{0.5}$	−0.79
$R_{ion} + 0.954 \bullet \chi^{-1}$	**0.96**

potential, U_{pred}.

One of the best options (1) with a strong linear dependence turned out to be a relatively simple one (Fig. 4**B**), while additional formulas are provided in Table S4:

$$U_{pred.} \sim [R_{ion} + 0.954 \bullet \chi^{-1}] \quad (1)$$

The physical explanation for this behavior is as follows: a larger ionic radius of the M dopant pushes oxygen atoms closer to tungsten, leading to a decrease in the W–O bond distance. This shorter bond distance increases the splitting of the t_{2g} orbital into bonding and antibonding states. The smaller the W–O bond distance, the greater the splitting, which lowers the energy of the bonding state and raises the W^{5+}/W^{6+} redox potential (vs. K^+/K). Regarding the influence of χ, a more electronegative metal M pulls more electron density away from the W–O bond and toward the dopant. This reduces the splitting of the t_{2g} level, raising its energy, which in turn lowers the redox potential.

3.4. DFT calculations

It has been repeatedly demonstrated that the use of hybrid functionals improves the accuracy of the average intercalation potential, bringing it into better agreement with experimental results [47]. However, due to the high computational cost of hybrid functionals, we had to use the smallest possible unit cell, which leads to an overestimation of the average potential. This overestimation arises from the inability to capture certain ordering effects that can only be described using much larger unit cells. For instance, cluster expansion calculations using the more computationally feasible PBE+*U* functional revealed the existence of an ordered $KNbWO_6$ (*Pma*2) phase with 36 atoms in the unit cell, yielding an average potential 0.2 V lower than the $KNbWO_6$ (*Imma*) phase, which has 18 atoms in the unit cell.

Assuming the correction provided by HSE06 is consistent across the smallest unit cell and larger cells, we derived a potential correction using small unit cells as $dE = E_{av}$(HSE06, small) - E_{av}(PBE+*U*, small), where E_{av} represents average intercalation potentials calculated with two different functionals. This correction is then applied to the average intercalation potential, E_{av}(PBE+*U*, cluster), obtained for the most stable ordered phase found with cluster expansion calculation, yielding E_{av}(corrected) = E_{av}(PBE+*U*, cluster) + *dE*. This represents our most accurate estimation of the average potential. The corresponding convex hulls and voltage curves calculated within PBE+*U* for all considered compositions are collected in Figures S9, S10.

The calculated average intercalation potentials using PBE+*U*, the hybrid HSE06 functional, and the corrected E_{av} are summarized in Table 2. The HSE06 functional predicts average potentials that are 0.2–0.5 V higher than those obtained with PBE+*U*. Both functionals indicate that Al-, Cr-, and Ti-doped materials have higher average potentials than Nb- and Ta-doped materials. This contrasts with the experimental evidence, which shows that Al, Cr, and Ti have lower potentials than Nb and Ta. However, the differences between these systems are small, falling below the accuracy limit of our calculations. Overall, the corrected E_{av} is reproduced within 0.1 V for Al, Ti, and Nb, and within 0.2 V for Cr and Ta relative to the E_{av} from the galvanostatic cycling results.

As for the redox mechanism, the analysis of magnetic moments from HSE06 calculations confirms W oxidation during deintercalation, with minor contributions from Cr and Ti. In $K_2Al_{0.33}W_{1.67}O_6$, W exhibits multiple intermediate oxidation states with magnetic moments of 0.1, 0.2, 0.3, 0.6, 0.7, and 1 μ_B. A similar situation is observed in $K_2Cr_{0.33}W_{1.67}O_6$. The magnetic moment on Cr is 2.9 μ_B corresponding to the high-spin 3+ state, which decreases to 2.7–2.8 μ_B upon deintercalation, indicating minor involvement of Cr in the redox process. In $K_2Ti_{0.5}W_{1.5}O_6$, the magnetic moments on W and Ti are 0.5 and 0.2 μ_B, respectively, but upon deintercalation, both moments drop to zero, suggesting some redox activity of Ti as well.

The local PDOS for the considered systems is shown in Fig. 5. In the case of Al-doped material, the absence of Al *d* orbitals results in no electronic density at the Fermi level, suggesting its poorest electronic conductivity among all cases. In contrast, for the Cr-doped material, the presence of *d*-PDOS in both the intercalated and deintercalated states highlights its metallic behavior and good electronic conductivity. The Ti-, Nb-, and Ta-doped materials exhibit very similar electronic structures, demonstrating metallic behavior in the fully intercalated state, with some electronic density at the Fermi level, and polaron-conduction in the fully deintercalated state with a band gap of approximately 3 eV. In this case, the difference in their electronic conductivity should be determined by the difference in small polaron migration barriers [48].

4. Discussion

The structural flexibility of AM_2O_6 defect pyrochlores offer broad opportunities for compositional tuning, especially through variations in the content and nature of the M metals. Therefore, the synthesis and electrochemical characterization of novel pyrochlore-based compounds present a promising avenue for energy storage science.

4.1. Future research prospects

While this work provides valuable insights on $KM_xW_{2-x}O_6$ electrochemical properties, it does not encompass the entire spectrum of possible dopants in tungsten-based defect pyrochlores. In particular, recent study on cesium analogues ($CsM_xW_{2-x}O_6$ [49]) has demonstrated compositions incorporating M metals with oxidation states spanning from +5 to +1. Some of the substituents are *d*-metals (*e.g.*, Ni^{2+}, Mn^{2+}, Fe^{3+}), which are responsible for the charge compensation mechanism of well-known cathode materials in metal-ion batteries (*e.g.*, layered

Table 2
Average intercalation potential E_{av} (V vs. K^+/K) calculated using PBE+*U* (U_{Nb} = 1.5 eV, U_{Cr} = 3.5 eV, U_W = 0 eV) and HSE06, and corrected value in comparison to the experimental values extracted from GC data.

Composition	E_{av} (PBE+*U*, small)	E_{av} (HSE06, small)	E_{av} (PBE+*U*, cluster)	E_{av} (corrected)	E_{av} (GC)
$K_2Al_{0.33}W_{1.67}O_6$ / $KAl_{0.33}W_{1.67}O_6$	1.13	1.41	0.77	1.05	1.12
$K_2Cr_{0.33}W_{1.67}O_6$ / $KCr_{0.33}W_{1.67}O_6$	1.27	1.54	1.08	1.35	1.15
$K_2Ti_{0.5}W_{1.5}O_6$ / $KTi_{0.5}W_{1.5}O_6$	1.12	1.60	0.79	1.27	1.22
K_2NbWO_6 / $KNbWO_6$	1.01	1.38	0.78	1.15	1.25
K_2TaWO_6 / $KTaWO_6$	0.94	1.29	0.72	1.07	1.31

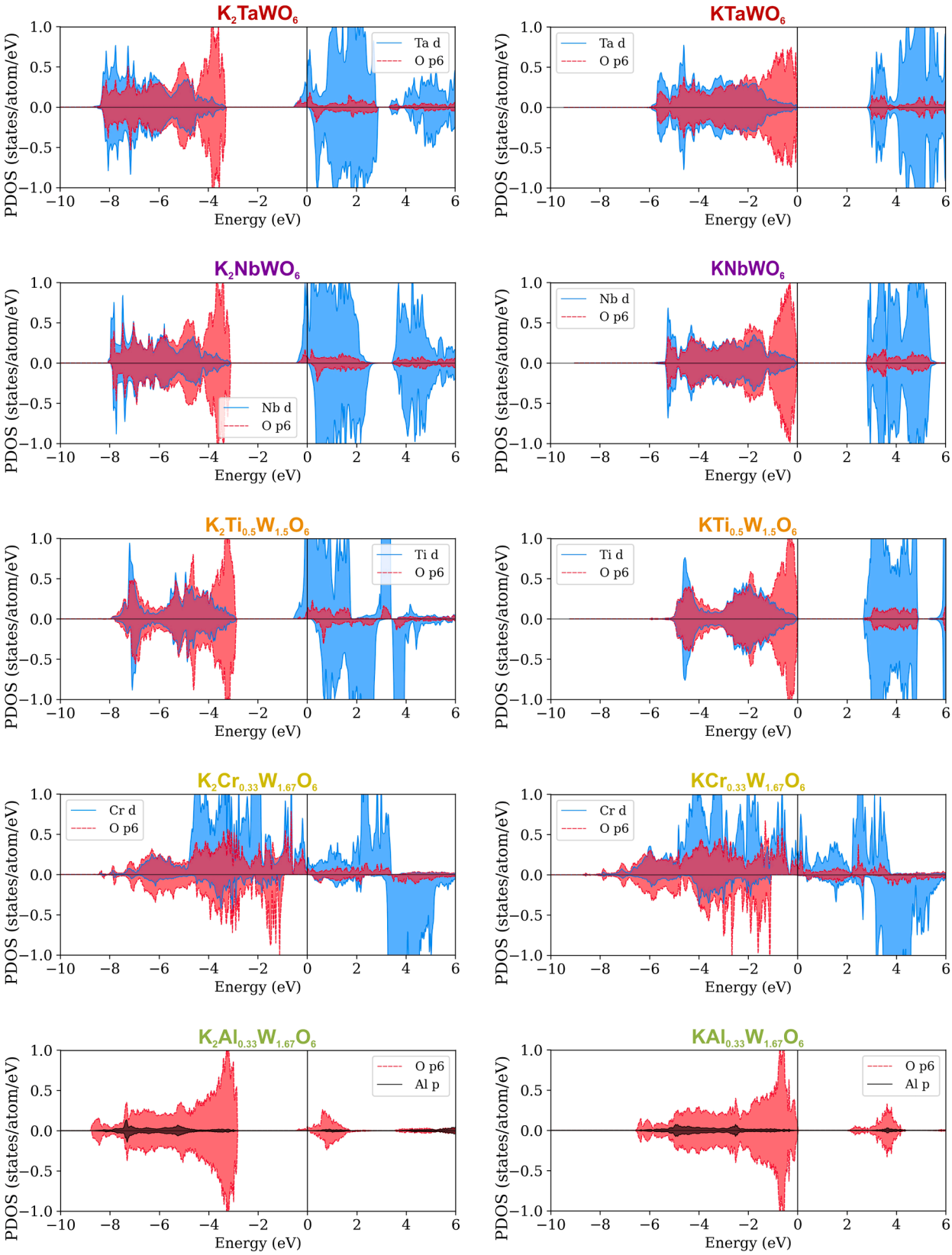

Fig. 5. Local partial density of states (PDOS) for non-equivalent M (M = Ta, Nb, Ti, Cr, Al) and six O atoms around metal (normalized) in $K_2M_xW_{2-x}O_6$ and $KM_xW_{2-x}O_6$ pyrochlores. The Fermi energy is at 0 eV.

oxides, Prussian blue analogues and etc.). If these dopants can be successfully introduced into $KM_xW_{2-x}O_6$, we can assume the additional electrochemical activity of pyrochlores at high potentials due to the possible redox transitions of such *d*-elements. This might allow us to reversibly cycle up to 2 potassium cations and increase the charge-discharge capacity of pyrochlores up to 2 times, respectively.

Besides $AM_xW_{2-x}O_6$ (A = alkali cation) structures, oxygen-deficient pyrochlores containing other redox-active 6+ cations (Te^{6+}, Mo^{6+} [50, 51]) also deserve investigation. Although $KNbTeO_6$ showed no evidence of Te^{6+}/Te^{4+} transitions during K (de)intercalation in half-cells [28], the electrochemical behavior of Mo in potassium pyrochlores remains unexplored due to the scarce information about $AM_xMo_{2-x}O_6$ synthesis. Therefore, expanding research into these systems could uncover new promising electrode materials for metal-ion batteries.

4.2. Structural features and potassium diffusion

A key structural feature of $KM_xW_{2-x}O_6$ pyrochlores is their three-dimensional isotropic K^+ migration network, as was shown recently for $KNbWO_6$ [28]. Interestingly, K can occupy multiple Wyckoff positions (8*b*, 16*d* and two types of 32*e* sites, Figure S11). The full set of positions were found for the $KNbWO_6$ pyrochlore in previous studies [32,43,44]. The reasons behind this split of sites is likely due to variations in synthesis conditions (*e.g.*, annealing time and heating/cooling rates). Moreover, the quality of the diffraction data and the refinement approaches (*e.g.*, using previously known structural models as starting points or manual placement of atoms according to Fourier maps) can also affect the obtained results. The superposition of K sites (Fig. 1**F**) creates a continuous 3D percolating system thus assuming high potassium diffusivity in the pyrochlore-based electrodes, as it was observed in other frameworks with split positions of mobile K^+ ions [52].

4.3. Electrochemical performance and electronic structure

Despite their structural similarities, the electrochemical performance of $KM_xW_{2-x}O_6$ pyrochlores varies greatly. The noticeable discrepancy likely stems from differences in the electronic structure of M^{x+}. With the exception of Al, all M dopants are transition elements with either filled (Nb^{5+}, Ta^{5+}), partially occupied (Cr^{3+}), or empty (Ti^{4+}) 3*d* shells. Therefore, $KNbWO_6$, $KTaWO_6$, and $KCr_{0.33}W_{1.67}O_6$ pyrochlores exhibit higher electronic conductivity and superior electrochemical stability in rate capability measurements (Fig. 2**D**) compared to $KTi_{0.5}W_{1.5}O_6$ and $KAl_{0.33}W_{1.67}O_6$. This assumption aligns well with the PDOS calculations (Fig. 5) of all pyrochlores except for $KTi_{0.5}W_{1.5}O_6$. The latter sample reveals worse performance in high-power tests relative to $KNbWO_6$ and $KTaWO_6$ despite their similar electronic structures. This contradiction may arise from the higher migration barriers of small polarons in the Ti-doped material.

4.4. Charge compensation mechanism

Recent study confirm that W^{6+}/W^{5+} couple primarily involves in the charge compensation mechanism during K (de)intercalation into the $KNbWO_6$ pyrochlore [28]. At the same time, the contribution of Nb^{5+}/Nb^{4+} pair was not confirmed by either theoretical calculations or electrochemical measurement of Te-based analogue ($KNbTeO_6$). While DFT results show minor electron transfer in Cr-doped and Ti-doped pyrochlores, it plays a negligible role in charge compensation, further underscoring W dominant redox activity across the $KM_xW_{2-x}O_6$ series.

4.5. Kinetic analysis of potassium storage mechanism

The *b* values from the CVs at different scan rates (Fig. 3) were calculated separately for redox peak currents and currents at low potentials for the following reasons. The redox peaks corresponds to a two-phase region on the *operando* PXRD map for $KNbWO_6$ [28]. Here, the phase boundary propagation is a rate-limiting factor. Such phase transforming materials can exhibit both slow diffusion and slow charge transfer contribution ("hybrid mode") to the alkali storage, which was also previously shown for the well-known $LiFePO_4$ cathode [53]. Meanwhile, the 0.8–1.3 V vs. K^+/K region with pseudocapacitance behavior correlates with the solid-solution region on the *operando* PXRD map [28]. It is worth noting that there are 3 mechanisms for the implementation of pseudocapacitance [54], including absorption-type (Pt, RHE), redox-type ($RuO_2 \times 0.5H_2O$), and intercalation-type (T-Nb_2O_5) pseudocapacitance. The last option is the most probable mechanism in the case of $KNbWO_6$.

4.6. Generalizing trends in $KM_xW_{2-x}O_6$ anode materials

The shape of cyclic voltammograms and charge-discharge curves for all $KM_xW_{2-x}O_6$ are similar. Therefore, the intercalation-type charge compensation mechanism is expected to be common for such compounds. Although the W^{6+}/W^{5+} couple is the proposed source of electrochemical activity in $KM_xW_{2-x}O_6$, the ~0.3 V shift in the AOP between $KAl_{0.33}W_{1.67}O_6$ and $KTaWO_6$ reflects structural adjustments (*e.g.*, M/W–O bond length) in pyrochlores. These changes induced by W substitution with M dopants. Since the fundamental characteristics of the dopants (ionic radius, electronegativity) differ, the electronic structure of pyrochlores and their electrochemical performance also vary.

5. Conclusion

To summarize, a series of $KM_xW_{2-x}O_6$ oxygen-deficient pyrochlores were investigated for the first time as novel negative electrode materials for potassium-ion batteries. The discovered shift in the average working potential (~1.1–1.3 V vs. K^+/K) upon changing the substituent (M) was analyzed based on the structural features of the pyrochlores and the intrinsic properties of the dopants. Regression analysis revealed a strong correlation between the experimentally observed average potential and the predicted values based on the ionic radius and electronegativity of the substituents. Variations in the electrochemical performance of $KM_xW_{2-x}O_6$ pyrochlores were linked to differences in the electronic structure of the M dopants and the resulting electronic conductivity of materials. These findings were also supported by theoretical calculations. The current study provides key points for future investigation into the electrochemical properties of defect pyrochlores for application in metal-ion batteries.

CRediT authorship contribution statement

Tashlanov Mikhail Yu.: Writing – original draft, Visualization, Methodology, Investigation, Formal analysis, Data curation, Conceptualization. **Aksyonov Dmitry A.:** Writing – original draft, Visualization, Software, Investigation, Formal analysis. **Marshenya Sergey N.:** Investigation, Formal analysis. **Mikheev Ivan V.:** Investigation. **Antipov Evgeny V.:** Validation, Supervision. **Fedotov Stanislav S.:** Validation, Supervision, Project administration, Conceptualization.

Declaration of Competing Interest

The authors declare that they have no known competing financial interests or personal relationships that could have appeared to influence the work reported in this paper.

Acknowledgments

The authors thank Alena I. Komayko for assistance with electrochemical measurements in a three-electrode cell and AICF of Skoltech for granting access to SEM facilities.

Appendix A. Supporting information

Supplementary data associated with this article can be found in the online version at doi:10.1016/j.jallcom.2025.180612.

Data availability

Data will be made available on request.

References

[1] S.S. Kalanur, I.-H. Yoo, I.-S. Cho, H. Seo, Effect of oxygen vacancies on the band edge properties of WO3 producing enhanced photocurrents, Electrochim. Acta 296 (2019) 517–527, https://doi.org/10.1016/j.electacta.2018.11.061.

[2] W. Wang, A. Janotti, C.G. Van De Walle, Role of oxygen vacancies in crystalline WO_3, J. Mater. Chem. C 4 (2016) 6641–6648, https://doi.org/10.1039/C6TC01643J.

[3] S.B. Upadhyay, R.K. Mishra, P.P. Sahay, Structural and alcohol response characteristics of Sn-doped WO3 nanosheets, Sens. Actuators B: Chem. 193 (2014) 19–27, https://doi.org/10.1016/j.snb.2013.11.049.

[4] S.S. Kalanur, H. Seo, Influence of molybdenum doping on the structural, optical and electronic properties of WO3 for improved solar water splitting, J. Colloid Interface Sci. 509 (2018) 440–447, https://doi.org/10.1016/j.jcis.2017.09.025.

[5] C. Huan, Z. Lu, S. Tang, Y. Cai, Q. Ke, Facile intercalation of alkali ions in WO3 for modulated electronic and optical properties: implications for artificial synapses and chromogenic application, Sci. China Phys. Mech. Astron 67 (2024) 227311, https://doi.org/10.1007/s11433-023-2224-8.

[6] S. Tosoni, C. Di Valentin, G. Pacchioni, Effect of alkali metals interstitial doping on structural and electronic properties of WO_3, J. Phys. Chem. C 118 (2014) 3000–3006, https://doi.org/10.1021/jp4123387.

[7] C. Dong, R. Zhao, L. Yao, Y. Ran, X. Zhang, Y. Wang, A review on WO3 based gas sensors: Morphology control and enhanced sensing properties, J. Alloy. Compd. 820 (2020) 153194, https://doi.org/10.1016/j.jallcom.2019.153194.

[8] C. Zhou, M. Wang, F. Yang, Gas sensing properties of WO3 based materials with hierarchical structural features, Ceram. Int. 50 (2024) 35869–35901, https://doi.org/10.1016/j.ceramint.2024.07.047.

[9] F. Wan, L. Li, C. Yao, K. Jiang, Z. Hu, N. Xu, J. Sun, J. Wu, Plasma assisted pulsed laser deposition of WO3 films for thermochromism, Mater. Chem. Phys. 314 (2024) 128880, https://doi.org/10.1016/j.matchemphys.2024.128880.

[10] S.J. Lee, D.S. Choi, S.H. Kang, W.S. Yang, S. Nahm, S.H. Han, T. Kim, VO_2 /WO_3 -based hybrid smart windows with thermochromic and electrochromic properties, ACS Sustain. Chem. Eng. 7 (2019) 7111–7117, https://doi.org/10.1021/acssuschemeng.9b00052.

[11] D. Chen, J. Ye, Hierarchical WO_3 hollow shells: dendrite, sphere, dumbbell, and their photocatalytic properties, Adv. Funct. Mater. 18 (2008) 1922–1928, https://doi.org/10.1002/adfm.200701468.

[12] E.K.H. Salje, Polaronic states and superconductivity in WO3-x, Condens. Matter 5 (2020) 32, https://doi.org/10.3390/condmat5020032.

[13] P.M. Wu, C. Hart, K. Luna, K. Munakata, A. Tsukada, S.H. Risbud, T.H. Geballe, M. R. Beasley, Synthesis and transport properties of superconducting thin films of K 0.33 WO 3: T c reduction due to disorder, Phys. Rev. B 89 (2014) 184501, https://doi.org/10.1103/PhysRevB.89.184501.

[14] Y. Xiao, M. Jiang, M. Cao, Developing WO3 as high-performance anode material for lithium-ion batteries, Mater. Lett. 285 (2021) 129129, https://doi.org/10.1016/j.matlet.2020.129129.

[15] C. Lian, X. Xiao, Z. Chen, Y. Liu, E. Zhao, D. Wang, C. Chen, Preparation of hexagonal ultrathin WO3 nano-ribbons and their electrochemical performance as an anode material in lithium ion batteries, Nano Res. 9 (2016) 435–441, https://doi.org/10.1007/s12274-015-0924-6.

[16] Y. Huang, R. Lu, M. Wang, J. Sakamoto, P.F.P. Poudeu, Hexagonal-WO3 nanorods encapsulated in nitrogen and sulfur co-doped reduced graphene oxide as a high-performance anode material for lithium ion batteries, J. Solid State Chem. 282 (2020) 121068, https://doi.org/10.1016/j.jssc.2019.121068.

[17] M. Rastgoo-Deylami, M. Javanbakht, H. Omidvar, K. Hooshyari, P. Salarizadeh, M. B. Askari, Nickel-doped monoclinic WO3 as high performance anode material for rechargeable lithium ion battery, J. Electroanal. Chem. 894 (2021) 115383, https://doi.org/10.1016/j.jelechem.2021.115383.

[18] S. Yoon, S.-G. Woo, K.-N. Jung, H. Song, Conductive surface modification of cauliflower-like WO3 and its electrochemical properties for lithium-ion batteries, J. Alloy. Compd. 613 (2014) 187–192, https://doi.org/10.1016/j.jallcom.2014.06.010.

[19] L. Hernan, M. Macias, J. Morales, L. Sanchez, J. Tirado, Lithium insertion into pyrochlore WO3, Solid State Ion. 48 (1991) 231–240, https://doi.org/10.1016/0167-2738(91)90037-C.

[20] A. Driouiche, M. Figlarz, C. Delmas, Lithium insertion in lacunar pyrochlore-type WO3, Solid State Ion. 62 (1993) 113–117, https://doi.org/10.1016/0167-2738(93)90258-5.

[21] Y. Liu, P.A. Russo, L.A. Montoro, N. Pinna, Recent developments in Nb-based oxides with crystallographic shear structures as anode materials for high-rate lithium-ion energy storage, Battery Energy 2 (2023) 20220037, https://doi.org/10.1002/bte2.20220037.

[22] C. Shen, S. Jiang, C. Ding, W. Xue, K. Xie, Lithium-ion diffusion path of tetragonal tungsten bronze (TTB) phase Nb18W16O93, Trans. Nonferrous Met. Soc. China 32 (2022) 3679–3686, https://doi.org/10.1016/S1003-6326(22)66048-5.

[23] W. Yao, H. Zhu, M. Wang, P. Li, P. Liu, P. Zou, A. Nie, G. Wang, F. Kang, C. Yang, Structural insights into the lithium ion storage behaviors of niobium tungsten double oxides, Chem. Mater. 34 (2022) 388–398, https://doi.org/10.1021/acs.chemmater.1c03727.

[24] A.L. Santhosha, S.K. Das, A.J. Bhattacharyya, Tungsten trioxide (WO_3) nanoparticles as a new anode material for sodium-ion batteries, J. Nanosci. Nanotechnol. 16 (2016) 4131–4135, https://doi.org/10.1166/jnn.2016.11786.

[25] F.J. García-García, J. Mosa, A.R. González-Elipe, M. Aparicio, Sodium ion storage performance of magnetron sputtered WO3 thin films, Electrochim. Acta 321 (2019) 134669, https://doi.org/10.1016/j.electacta.2019.134669.

[26] S. Chu, M. Yu, B. Liu, T. Lu, Z. Hou, Y. Qu, F. Zeng, WO3-x@W2N heterogeneous nanorods cross-linked in carbon nanosheets for electrochemical potassium storage, Chem. Eng. J. 435 (2022) 135188, https://doi.org/10.1016/j.cej.2022.135188.

[27] C. Chen, H. Zhu, M. Shi, L. Hu, Z. Xue, H. Ye, L. Zhao, C. Yan, Oxygen vacancies-modulated tungsten oxide anode for ultra-stable and fast aqueous aluminum-ion storage, Energy Storage Mater. 49 (2022) 370–379, https://doi.org/10.1016/j.ensm.2022.04.013.

[28] M.Yu Tashlanov, S.N. Marshenya, A.A. Golubnichiy, D.A. Aksyonov, E.V. Antipov, S.S. Fedotov, Low-strain, long-life and high-power K-ion anode material enabled by a pyrochlore-type framework with facile 3D isotropic diffusion, J. Power Sources 629 (2025) 236042, https://doi.org/10.1016/j.jpowsour.2024.236042.

[29] M. Subramanian, R. Subramanian, A. Clearfield, Fast ion conduction in the defect pyrochlore system KBxW2−xO6(B = Al, Ti and Ta), Solid State Ion. 15 (1985) 15–19, https://doi.org/10.1016/0167-2738(85)90101-8.

[30] A.I. Komayko, S.V. Ryazantsev, I.A. Trussov, N.A. Arkharova, D.E. Presnov, E. E. Levin, V.A. Nikitina, The misconception of Mg^{2+} insertion into prussian blue analogue structures from aqueous solution, ChemSusChem 14 (2021) 1574–1585, https://doi.org/10.1002/cssc.202002916.

[31] V. Petříček, M. Dušek, L. Palatinus, Crystallographic computing system JANA2006: general features, Z. F. üR. Krist. - Cryst. Mater. 229 (2014) 345–352, https://doi.org/10.1515/zkri-2014-1737.

[32] D. Babel, G. Pausewang, W. Viebahn, Notizen: Die Struktur einiger fluoride, oxide und oxidfluoride AMe $_2$ X $_6$: Der RbNiCrF $_6$ -Typ, Z. F. üR. Naturforsch. B 22 (1967) 1219–1220, https://doi.org/10.1515/znb-1967-1126.

[33] K. Momma, F. Izumi, *VESTA*: a three-dimensional visualization system for electronic and structural analysis, J. Appl. Crystallogr 41 (2008) 653–658, https://doi.org/10.1107/S0021889808012016.

[34] A. Tonda, Review of PySR: high-performance symbolic regression in Python and Julia, Genet Program Evol. Mach. 26 (2025) 7, https://doi.org/10.1007/s10710-024-09503-4.

[35] E.E. Nazarov, O.A. Tyablikov, V.A. Nikitina, E.V. Antipov, S.S. Fedotov, Polyacrylonitrile-derived carbon nanocoating for long-life high-power phosphate electrodes, Appl. Nano 4 (2023) 25–37, https://doi.org/10.3390/applnano4010002.

[36] N.S. Katorova, S.S. Fedotov, D.P. Rupasov, N.D. Luchinin, B. Delattre, Y.-M. Chiang, A.M. Abakumov, K.J. Stevenson, Effect of concentrated diglyme-based electrolytes on the electrochemical performance of potassium-ion batteries, ACS Appl. Energy Mater. 2 (2019) 6051–6059, https://doi.org/10.1021/acsaem.9b01173.

[37] A.I. Komayko, N.A. Arkharova, D.E. Presnov, E.E. Levin, V.A. Nikitina, Resolving the seeming contradiction between the superior rate capability of Prussian blue analogues and the extremely slow ionic diffusion, J. Phys. Chem. Lett. 13 (2022) 3165–3172, https://doi.org/10.1021/acs.jpclett.2c00482.

[38] G. Kresse, J. Furthmüller, Efficiency of ab-initio total energy calculations for metals and semiconductors using a plane-wave basis set, Comput. Mater. Sci. 6 (1996) 15–50, https://doi.org/10.1016/0927-0256(96)00008-0.

[39] D.A. Aksyonov, S.S. Fedotov, K.J. Stevenson, A. Zhugayevych, Understanding migration barriers for monovalent ion insertion in transition metal oxide and phosphate based cathode materials: a DFT study, Comput. Mater. Sci. 154 (2018) 449–458, https://doi.org/10.1016/j.commatsci.2018.07.057.

[40] J.P. Perdew, K. Burke, M. Ernzerhof, Generalized gradient approximation made simple, Phys. Rev. Lett. 77 (1996) 3865–3868, https://doi.org/10.1103/PhysRevLett.77.3865.

[41] S.L. Dudarev, G.A. Botton, S.Y. Savrasov, C.J. Humphreys, A.P. Sutton, Electron-energy-loss spectra and the structural stability of nickel oxide: an LSDA+U study, Phys. Rev. B 57 (1998) 1505–1509, https://doi.org/10.1103/PhysRevB.57.1505.

[42] A. Van De Walle, M. Asta, G. Ceder, The alloy theoretic automated toolkit: a user guide, Calphad 26 (2002) 539–553, https://doi.org/10.1016/S0364-5916(02)80006-2.

[43] P.W. Barnes, P.M. Woodward, Y. Lee, T. Vogt, J.A. Hriljac, Pressure-induced cation migration and volume expansion in the defect pyrochlores $ANbWO_6$ (A = NH_4^+, Rb^+, H^+, K^+, J. Am. Chem. Soc. 125 (2003) 4572–4579, https://doi.org/10.1021/ja0292187.

[44] D. Murphy, R. Cava, K. Rhyne, R. Roth, A. Santoro, S. Zahurak, J. Dye, Structural aspects of insertion reactions of the pyrochlore, KNbWO6, Solid State Ion. 18–19 (1986) 799–801, https://doi.org/10.1016/0167-2738(86)90265-1.

[45] A.D. Dembitskiy, D.A. Aksyonov, A.M. Abakumov, S.S. Fedotov, NH+ -based frameworks as a platform for designing electrodes and solid electrolytes for Na-ion batteries: a screening approach, Solid State Ion. 374 (2022) 115810, https://doi.org/10.1016/j.ssi.2021.115810.

[46] R. Kumar, M. Bag, Quantifying capacitive and diffusion-controlled charge storage from 3D Bulk to 2D layered halide perovskite-based porous electrodes for efficient

supercapacitor applications, J. Phys. Chem. C. 125 (2021) 16946–16954, https://doi.org/10.1021/acs.jpcc.1c05493.

[47] I. Timrov, F. Aquilante, M. Cococcioni, N. Marzari, Accurate electronic properties and intercalation voltages of olivine-type Li-Ion cathode materials from extended hubbard functionals, PRX Energy 1 (2022) 033003, https://doi.org/10.1103/PRXEnergy.1.033003.

[48] D.A. Aksyonov, A.O. Boev, S.S. Fedotov, A.M. Abakumov, Computational insights into ionic conductivity of transition metal electrode materials for metal-ion batteries - a review, Solid State Ion. 393 (2023) 116170, https://doi.org/10.1016/j.ssi.2023.116170.

[49] M. Weiss, G. Hoerner, B. Weber, R. Marschall, The elemental multifariousness of the defect-pyrochlore crystal structure and application in photocatalytic hydrogen generation, Energy Tech. 10 (2022) 2100302, https://doi.org/10.1002/ente.202100302.

[50] D.G. Fukina, A.S. Ganov, A.V. Boryakov, A.V. Koroleva, E.V. Zhizhin, D.N. Titaev, E.V. Shilova, E.V. Suleimanov, Electron structure and photocatalytic activity of new compounds $CsM_xW2\text{-}xO_6$ (M = Sn, V and Mo, x=0–0.5) with β-pyrochlore structure, J. Solid State Chem. 337 (2024) 124803, https://doi.org/10.1016/j.jssc.2024.124803.

[51] A.V. Knyazev, W. Paraguassu, A.G. Blokhina, M.I. Lelet, S.S. Knyazeva, G.B. Corrêa Junior, Thermodynamic and spectroscopic properties of $KNbTeO_6$, J. Chem. Thermodyn. 107 (2017) 26–36, https://doi.org/10.1016/j.jct.2016.12.013.

[52] V. Ramezankhani, N.D. Luchinin, S.N. Marshenya, M.V. Zakharkin, A. A. Golubnichiy, A.V. Morozov, O. Emilianova, K.J. Stevenson, E.V. Antipov, A. M. Abakumov, S.S. Fedotov, Exploring $KTiPO_4F$ as a robust polyanion anode material for potassium-ion batteries, J. Mater. Chem. A (2024), https://doi.org/10.1039/D3TA08103F.

[53] V.D. Sumanov, O.A. Tyablikov, A.V. Morozov, S.S. Fedotov, S.Y. Vassiliev, V. A. Nikitina, Phase boundary propagation mode in nano-sized electrode materials evidenced by potentiostatic current transients analysis: Li-rich $LiFePO_4$ case study, Electrochim. Acta 368 (2021) 137627, https://doi.org/10.1016/j.electacta.2020.137627.

[54] S. Fleischmann, J.B. Mitchell, R. Wang, C. Zhan, D. Jiang, V. Presser, V. Augustyn, Pseudocapacitance: from fundamental understanding to high power energy storage materials, Chem. Rev. 120 (2020) 6738–6782, https://doi.org/10.1021/acs.chemrev.0c00170.